2024 IEEE International Conference on Robotics and Automation (ICRA 2024)
May 13-17, 2024. Yokohama, Japan

Robust Model Predictive Control with Control Barrier Functions for Autonomous Surface Vessels

Wei Wang*, Wei Xiao*, Alejandro Gonzalez-Garcia*, Jan Swevers, Carlo Ratti and Daniela Rus

***Abstract*— In autonomous robot navigation, the trajectories from path planners are considered to be safe regions, and deviations could endanger vessels. Model Predictive Control (MPC) stands as a popular choice for trajectory tracking problems as it naturally addresses operational constraints, such as dynamics and control constraints. Nevertheless, achieving robustness in changing environments like oceans and rivers, which are constantly subject to significant external disturbances, remains an ongoing challenge for MPC. It must consistently keep the system within a predefined safe region (such as a reference trajectory) even in the presence of model inaccuracies and perturbations. To address this challenge, we present a robust model predictive control strategy utilizing Control Barrier Functions (CBFs), which increases the disturbance-rejection abilities. We verify our method on an autonomous surface vessel in simulation and natural waters, both with external disturbances. Specifically, compared with the traditional MPC method, our proposed MPC-CBF strategy reduces tracking errors by 17.82% and 40.26% in simulations and field experiments, respectively. Although the control effort slightly increases by 7.78% and 4.20%, respectively, these results clearly demonstrate the enhanced resilience of MPC-CBF to disturbances.**

I. Introduction

Due to a variety of applications like marine transportation, bathymetry, search and rescue, disaster management, and oceanic exploration, Autonomous Surface Vessels (ASVs) have attracted attention in both industrial and academic communities [1]–[7]. Trajectory tracking is an essential component for ASVs to perform time-sensitive tasks such as dynamic obstacle avoidance, and multi-robot coordination.

The safety of both the vessel and its passengers or goods plays a crucial role in ensuring the success of autonomous operations. Maintaining proximity to planned trajectories and adhering to time constraints is of paramount importance, as any deviations have the potential to lead to collisions or undesirable behavior in dynamic environments. Nevertheless, factors such as model uncertainty and external disturbances arising from wind, waves, and currents pose a significant threat to the control of ASVs. Various approaches have been proposed to enhance robustness, consequently mitigating deviations in the face of these disturbances and uncertainties, e.g., sliding mode-based controllers [8]–[10] and data-driven algorithms [11], [12].

A popular control system strategy within the robotics field is model predictive control (MPC). MPC utilizes model knowledge and multi-objective optimization to minimize tracking error, control effort, and factor system constraints. MPC has been successfully used for ASV trajectory tracking [6], [13], [14], achieving low tracking error and control effort. However, MPC can be affected by model errors and external disturbances, and the computational complexity increases significantly as constraints increase.

To reduce computational complexity, the Control Barrier Function (CBF) method has been widely adopted as an extension or alternative to MPC. Barrier functions (BFs) are Lyapunov-like functions [15], [16], whose use can be traced back to optimization problems [17]. CBFs, on the other hand, represent an extension of BFs tailored for control systems. They translate a constraint defined in terms of system states into a constraint on the control inputs. CBFs offer a state-feedback controller that is rigorously proven to be safe while remaining computationally efficient. Specifically, CBFs are well-suited for constraints characterized by a relative degree of one concerning the system dynamics [18], [19]. The High Order CBF (HOCBF), as proposed in [20] and [21], is designed to effectively handle constraints with arbitrarily high relative degrees, making it a versatile extension of the conventional CBF framework. Robust CBFs to account for perturbations have also been extensively studied in the CBF framework [22].

This paper proposes to combine MPC and HOCBFs, in the context of ASV trajectory tracking subject to external disturbances. The HOCBFs are introduced to enforce safety constraints on the system state, steering the vessel towards a boundary of the predefined trajectory. The main contributions of this work include:

- An MPC-CBF framework for ASV trajectory tracking;
- CBFs/HOCBFs for trajectory tracking under perturbations, instead of their traditional use for obstacle avoidance;
- An extensive study of numerical simulations subject to increasing model-based environmental disturbances;
- Field experiments with an ASV, verifying the effectiveness of the MPC-CBF framework;

This work was supported by a grant from the Amsterdam Institute for Advanced Metropolitan Solutions (AMS) in Netherlands, and by the MIT-Belgium - KU Leuven Seed Fund from MIT International Science and Technology Initiatives (MISTI). A. Gonzalez-Garcia was supported by the Flanders Make SBO project ARENA (Agile & Reliable Navigation).

W. Wang, W. Xiao, and D. Rus are with the Computer Science and Artificial Intelligence Lab (CSAIL), Massachusetts Institute of Technology, Cambridge, MA 02139 USA. {wweiwang, weixy, rus}@mit.edu

W. Wang, and C. Ratti are with the SENSEable City Laboratory, Massachusetts Institute of Technology, Cambridge, MA 02139 USA. {wweiwang, ratti}@mit.edu

W. Wang is with the Marine Robotics Lab, Department of Mechanical Engineering, College of Engineering, University of Wisconsin-Madison, Madison, WI 53706 USA. {wwang745}@wisc.edu

A. Gonzalez-Garcia, and J. Swevers are with MECO Research Team, Department of Mechanical Engineering, KU Leuven, Belgium and Flanders Make@KU Leuven, Belgium. {alex.gonzalezgarcia, jan.swevers}@kuleuven.be

*These authors contributed equally to this work.

• A comparative analysis between MPC-CBF and MPC, illustrating the increased robustness to disturbances of MPC-CBF.

II. ASV Overview and Preliminaries

In this section, we introduce the ASV prototype, its dynamic model, and some preliminary concepts. The dynamic model introduced here will serve as the foundation for the MPC-CBF design in subsequent section.

A. Surface Vessel

The vessel has four thrusters around the hull to achieve holonomic motions as shown in Fig. 1. The primary controller for the system is an Intel NUC running the Robot Operating System (ROS). Additionally, for real-time actuator control, an auxiliary microprocessor (STM32F103) is incorporated. The surface vessel is equipped with a range of onboard sensors, including a 3D LiDAR (Velodyne, Puck VLP-16), and an IMU. The vessel weighs approximately 15 kg and has dimensions of 0.90 m in length, 0.45 m in width, and 0.15 m in height. Power is supplied by an 11.1 V Li-Po battery, offering an operational duration of approximately three hours. For more detailed information on the surface vessel, refer to [13].

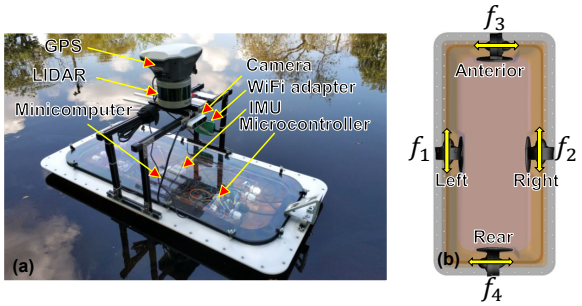

Fig. 1. The surface vessel. (a) Prototype (side view); (b) thruster configuration (bottom view). f_1, f_2, f_3 and f_4 denote the forces generated by left, right, anterior and rear thrusters, respectively.

B. ASV Dynamics

We establish two coordinate systems to describe the vessel: the inertial frame denoted as OXY and the body-fixed frame represented as $o_b x_b y_b$. The dynamic model for the vessel is described by the following nonlinear differential equation, as detailed in [13]:

$$\dot{\boldsymbol{\eta}} = \mathbf{R}(\boldsymbol{\eta})\mathbf{v} \tag{1}$$

$$\mathbf{M}\dot{\mathbf{v}} + \mathbf{C}(\mathbf{v})\mathbf{v} + \mathbf{D}(\mathbf{v})\mathbf{v} = \boldsymbol{\tau} + \boldsymbol{\tau}_{\text{env}} \tag{2}$$

where $\boldsymbol{\eta} = [x \quad y \quad \psi]^T \in \mathbb{R}^3$ denotes the pose, comprising position and heading, of the vessel in the inertial frame; $\mathbf{v} = [u \quad v \quad r]^T \in \mathbb{R}^3$ represents the vessel's velocity in the body-fixed frame; $\mathbf{R}(\boldsymbol{\eta}) \in \mathbb{R}^{3\times3}$ stands for the rotation matrix, which expresses the transformation from the body-fixed frame to the inertial frame; $\mathbf{M} \in \mathbb{R}^{3\times3}$ represents the symmetric positive-definite added mass and inertia matrix ; $\mathbf{C}(\mathbf{v}) \in \mathbb{R}^{3\times3}$ represents the skew-symmetric matrix accounting for the Coriolis and centripetal forces; $\mathbf{D}(\mathbf{v}) \in \mathbb{R}^{3\times3}$ represents the positive-semi-definite drag matrix; $\boldsymbol{\tau} = [\tau_u \quad \tau_v \quad \tau_r]^T \in \mathbb{R}^3$ represents the total force and torque applied by the thrusters; $\boldsymbol{\tau}_{\text{env}} \in \mathbb{R}^3$ characterizes environmental disturbances stemming from factors such as currents, waves, and winds. More specifically, $\mathbf{M}$, $\mathbf{C}(\mathbf{v})$ and $\mathbf{D}(\mathbf{v})$ can be further elaborated as follows:

$$\mathbf{M} = \text{diag}\{m_{11}, m_{22}, m_{33}\}, \tag{3}$$

$$\mathbf{C}(\mathbf{v}) = \begin{bmatrix} 0 & 0 & -m_{22}v \\ 0 & 0 & m_{11}u \\ m_{22}v & -m_{11}u & 0 \end{bmatrix}, \tag{4}$$

$$\mathbf{D}(\mathbf{v}) = \text{diag}\{X_u, Y_v, N_r\}. \tag{5}$$

$\boldsymbol{\tau}$ is mathematically defined as follows:

$$\boldsymbol{\tau} = \mathbf{B}\mathbf{u} = \begin{bmatrix} 1 & 1 & 0 & 0 \\ 0 & 0 & 1 & 1 \\ \frac{a_\text{d}}{2} & -\frac{a_\text{d}}{2} & \frac{b_\text{d}}{2} & -\frac{b_\text{d}}{2} \end{bmatrix} \begin{pmatrix} f_1 \\ f_2 \\ f_3 \\ f_4 \end{pmatrix} \tag{6}$$

where $\mathbf{B} \in \mathbb{R}^{4\times3}$ represents the control matrix, defining the arrangement of the thrusters, $\mathbf{u} = [f_1 \quad f_2 \quad f_3 \quad f_4]^T \in \mathbb{R}^4$ represents the control vector, where f_1, f_2, f_3, and f_4 correspond to the forces generated by the left, right, anterior, and rear thrusters, respectively. a_d is the distance between the main thrusters (left and right thrusters) and b_d is the distance between the tunnel thrusters (anterior and rear thrusters). The specific configuration of the four thrusters is illustrated in Fig. 1.

By merging (1) and (2), we can reformulate the dynamic model as follows:

$$\dot{\mathbf{x}} = f(\mathbf{x}) + g(\mathbf{x})\mathbf{u} + \mathbf{w} \tag{7}$$

where $f(\mathbf{x}) = [\mathbf{0}_{3\times3} \quad \mathbf{R}(\boldsymbol{\eta}); \mathbf{0}_{3\times3} \quad -\mathbf{M}^{-1}(\mathbf{C}(\mathbf{v}) + \mathbf{D}(\mathbf{v}))]$, $g(\mathbf{x}) = [\mathbf{0}_{3\times4}; \mathbf{M}^{-1}\mathbf{B}]$, $\mathbf{w} = [\mathbf{0}_{3\times1}; \mathbf{M}^{-1}\boldsymbol{\tau}_{\text{env}}]$. Moreover, the state vector $\mathbf{x}(t) \in \mathbb{R}^{n_q}$ and the control vector $\mathbf{u}(t) \in \mathbb{R}^{n_u}$ are defined as follows:

$$\mathbf{x} = [x \quad y \quad \psi \quad u \quad v \quad r]^T, \tag{8}$$

$$\mathbf{u} = [f_1 \quad f_2 \quad f_3 \quad f_4]^T. \tag{9}$$

The system model (7) defines how the state $\mathbf{x}$ evolves with the control input $\mathbf{u}$.

C. High Order Control Barrier Functions

We briefly introduce the concept of high order CBFs in this section, and we start with some definitions for CBFs/HOCBFs. Consider an affine control system:

$$\dot{\mathbf{x}} = f(\mathbf{x}) + g(\mathbf{x})\mathbf{u} \tag{10}$$

where $\mathbf{x} \in X \subset \mathbb{R}^n$, $f : \mathbb{R}^n \to \mathbb{R}^n$ and $g : \mathbb{R}^n \to \mathbb{R}^{n\times q}$ are Lipschitz continuous, and $\mathbf{u} \in U \subset \mathbb{R}^q$ is the control constraint set.

Definition 1: A set $C \subset \mathbb{R}^n$ is forward invariant for system (10) if its solutions for some controller $\mathbf{u} \in U$ starting at any $\mathbf{x}(0) \in C$ satisfy $\mathbf{x}(t) \in C$, $\forall t \geq 0$.

***Definition** 2:* (*Relative degree* [23]) The relative degree of a (sufficiently many times) differentiable function $b:\mathbb{R}^n \to \mathbb{R}$ with respect to (10) is the number of times it needs to be differentiated along its dynamics until any component of the control $\mathbf{u}$ explicitly shows in the corresponding derivative.

Since function b is used to define a constraint $b(\mathbf{x}) \geq 0$, we will also refer to the relative degree of b as the relative degree of the constraint. For a constraint $b(\mathbf{x}) \geq 0$ with relative degree m, $b:\mathbb{R}^n \to \mathbb{R}$, and $\psi_0(\mathbf{x}) := b(\mathbf{x})$, we define a sequence of functions $\psi_i:\mathbb{R}^n \to \mathbb{R}, i \in \{1,\dots,m\}$:

$$\psi_i(\mathbf{x}) := \dot{\psi}_{i-1}(\mathbf{x}) + \alpha_i(\psi_{i-1}(\mathbf{x})), i \in \{1,\dots,m\}, \tag{11}$$

where $\alpha_i(\cdot), i \in \{1,\dots,m\}$ denotes a $(m-i)^{th}$ order differentiable class $\mathscr{K}$ function.

We further define a sequence of sets $C_i, i \in \{1,\dots,m\}$ associated with (11) in the form:

$$C_i := \{\mathbf{x} \in \mathbb{R}^n : \psi_{i-1}(\mathbf{x}) \geq 0\}, i \in \{1,\dots,m\}. \tag{12}$$

***Definition** 3:* (*High Order Control Barrier Function (HOCBF)* [20]) Let $C_1,\dots,C_m$ be defined by (12) and $\psi_1(\mathbf{x}),\dots,\psi_m(\mathbf{x})$ be defined by (11). A function $b:\mathbb{R}^n \to \mathbb{R}$ is a High Order Control Barrier Function (HOCBF) of relative degree m for system (10) if there exist $(m-i)^{th}$ order differentiable class $\mathscr{K}$ functions $\alpha_i, i \in \{1,\dots,m-1\}$ and a class $\mathscr{K}$ function α_m such that

$$\sup_{\mathbf{u}\in U}[L_f^m b(\mathbf{x}) + L_g L_f^{m-1} b(\mathbf{x})\mathbf{u} + O(b(\mathbf{x})) + \alpha_m(\psi_{m-1}(\mathbf{x}))] \geq 0, \tag{13}$$

for all $\mathbf{x} \in C_1 \cap,\dots,\cap C_m$. In (13), the left part is actually $\psi_m(\mathbf{x})$, L_f, L_g denote Lie derivatives along f and along g, respectively, and $O(b(\mathbf{x})) = \sum_{i=1}^{m-1} L_f^i(\alpha_{m-i} \circ \psi_{m-i-1})(\mathbf{x})$.

The HOCBF is a general form of the relative degree one CBF [18], [19], i.e., setting $m = 1$ reduces the HOCBF to the common CBF form: $L_f b(\mathbf{x}) + L_g b(\mathbf{x})\mathbf{u} + \alpha_1(b(\mathbf{x})) \geq 0$.

Theorem 1: ([20]) Given an HOCBF $b(\mathbf{x})$ from Def. 3 with the associated sets $C_1,\dots,C_m$ defined by (12), if $\mathbf{x}(0) \in C_1 \cap,\dots,\cap C_m$, then any Lipschitz continuous controller $\mathbf{u}(t) \in U$ that satisfies the constraint in (13), $\forall t \geq 0$ renders $C_1 \cap,\dots,\cap C_m$ forward invariant for system (10).

CBFs/HOCBFs are commonly employed to transform constrained optimal control problems onto quadratic programs that are very efficient to solve [18]. They are used to guarantee system safety. However, in this paper, we use CBFs/HOCBFs to achieve trajectory tracking for surface vessels under perturbations.

III. Robust Model Predictive Control via Control Barrier Functions

In this section, we establish a mathematical formulation for the trajectory tracking problem and subsequently design an MPC-CBF scheme to address the problem, considering robustness and optimality in the solution.

A. Trajectory Tracking Problem Formulation

Trajectory tracking is concerned with the design of control laws that force a mobile robot to converge to a time-parameterized reference. Trajectory tracking usually requires the robot to track the specified pose and velocity defined at each given time. The reference trajectory which is parameterized at each time step k can be formulated as follows:

$$\mathbf{x}_k^{\text{ref}} = [x_k^{\text{r}} \;\; y_k^{\text{r}} \;\; \psi_k^{\text{r}} \;\; u_k^{\text{r}} \;\; v_k^{\text{r}} \;\; r_k^{\text{r}}]^T \tag{14}$$

We then establish the tracking error at each time step k as $\mathbf{e}_k = [x_k^{\text{e}} \;\; y_k^{\text{e}} \;\; \psi_k^{\text{e}} \;\; u_k^{\text{e}} \;\; v_k^{\text{e}} \;\; r_k^{\text{e}}]^T$ as the disparity between the reference state and actual state of the vessel. The objective of the trajectory tracking problem here is to design appropriate control laws for the four thrusters with the aim of driving $\mathbf{e}_k$ to zero at each time step.

B. Nonlinear Model Predictive Control Design

For our trajectory tracking problem, we formulate the optimal control problem for MPC in the form of a least square function to penalize the deviations of predicted state ($\mathbf{x}_k$) and control ($\mathbf{u}_k$) trajectories from their specified references, over the given prediction horizon window N_c ($t_j \leq t \leq t_{j+N_c}$):

$$\min_{\mathbf{x}_k,\mathbf{u}_k} \frac{1}{2}\Big\{ \sum_{k=j}^{j+N_c-1} (\|\mathbf{x}_k - \mathbf{x}_k^{\text{ref}}\|_{W_q}^2 + \|\mathbf{u}_k\|_{W_u}^2) + \|\mathbf{x}_{N_c} - \mathbf{x}_{N_c}^{\text{ref}}\|_{W_{N_c}}^2 \Big\} \tag{15a}$$

$$\text{s.t.} \quad \mathbf{x}_j = \hat{\mathbf{x}}_j, \tag{15b}$$

$$\mathbf{x}_{k+1} = f(\mathbf{x}_k) + g(\mathbf{x}_k)\mathbf{u}_k, k = j,\cdots,j+N_c-1, \tag{15c}$$

$$\mathbf{x}_{k,\min} \leq \mathbf{x}_k \leq \mathbf{x}_{k,\max}, k = j,\cdots,j+N_c, \tag{15d}$$

$$\mathbf{u}_{k,\min} \leq \mathbf{u}_k \leq \mathbf{u}_{k,\max}, k = j,\cdots,j+N_c-1, \tag{15e}$$

where $\mathbf{x}_k \in \mathbb{R}^{n_q}$ denotes the vessel state, $\mathbf{u}_k \in \mathbb{R}^{n_u}$ denotes the control input, $\hat{\mathbf{x}}_j \in \mathbb{R}^{n_q}$ denotes the current state estimate, $\mathbf{x}_k^{\text{ref}}$ and $\mathbf{u}_k^{\text{ref}}$ denote the time-varying state and control references, respectively; $\mathbf{x}_{N_c}^{\text{ref}}$ denotes the terminal state reference; $W_q \in \mathbb{R}^{n_q \times n_q}$, $W_u \in \mathbb{R}^{n_u \times n_u}$, and $W_{N_c} \in \mathbb{R}^{n_q \times n_q}$ are the positive definite weight matrices that penalize deviations from the desired values. Furthermore, $\mathbf{x}_{k,\min}$ and $\mathbf{x}_{k,\max}$ denote the lower and upper bounds of the states, respectively; $\mathbf{u}_{k,\min}$ and $\mathbf{u}_{k,\max}$ denote the lower and upper bounds of the control input, respectively.

The weighting matrices W_q, W_u and W_{N_c} for the MPC used in the experiments are selected as

$$W_q = \text{diag}\{20,20,10,10,10,10\}, \tag{16}$$

$$W_{N_c} = \text{diag}\{100,100,50,50,50,50\}, \tag{17}$$

$$W_u = \text{diag}\{1,1,1,1\}. \tag{18}$$

A sufficiently large terminal penalty matrix could improve the stability of the MPC algorithm. The prediction horizon was chosen as $N_c = 4$ s, with a sampling time of 0.1 s, and the constraints on the control input $\mathbf{u}$ used in the experiments are chosen as follow

$$\mathbf{u}_{k,\max} = [\mathbf{6}_{4\times1}] \text{ N} \;;\; \mathbf{u}_{k,\min} = -[\mathbf{6}_{4\times1}] \text{ N} \tag{19}$$

Our implementation of the MPC controller is realized using the open-source ACADO toolkit [24].

C. Robust Control Barrier Function

In scenarios subject to model inaccuracies or external perturbations, MPC may lose constraint satisfaction guarantees, and tracking accuracy. To address this, we propose to use CBFs/HOCBFs to equip MPC with guarantees. In the ASV case, the dynamics (10) have different forms of perturbations. Thus, the ASV model is extended with an additive term $\mathbf{w} \in \mathbb{R}^n$ as follows:

$$\dot{\mathbf{x}} = f(\mathbf{x}) + g(\mathbf{x})\mathbf{u} + \mathbf{w}, \tag{20}$$

where the perturbations are assumed to be bounded such that $|\mathbf{w}| \leq \mathbf{w}$ (inequality interpreted componentwise), $\mathbf{w} \in \mathbb{R}^n$.

A robust CBF [22] for system (20) should satisfy the following CBF constraint:

$$L_f b(\mathbf{x}) + L_g b(\mathbf{x})\mathbf{u} + \alpha_1(b(\mathbf{x})) - \left|\frac{db(\mathbf{x})}{d\mathbf{x}}\right| \mathbf{w} \geq 0. \tag{21}$$

The satisfaction of the above constraint implies the satisfaction of $L_f b(\mathbf{x}) + L_g b(\mathbf{x})\mathbf{u} + \alpha_1(b(\mathbf{x})) + \frac{db(\mathbf{x})}{d\mathbf{x}}\mathbf{w} \geq 0$, and thus, we can provably show the satisfaction of $b(\mathbf{x}) \geq 0$ using the classic CBF theory. We can define robust HOCBFs based on (21) as in (11) and Def. 3.

Now, we focus on how to design HOCBFs for the robust trajectory tracking control of the surface vessel. Suppose the reference trajectory is defined by $h(\mathbf{x}) = 0$, where $h : \mathbb{R}^n \to \mathbb{R}$ is continuously differentiable. We can define a tube (a safe tracking state space) using two robust HOCBFs:

$$\begin{aligned} b_1(\mathbf{x}) &= h(\mathbf{x}) - c, \\ b_2(\mathbf{x}) &= -h(\mathbf{x}) - c, \end{aligned} \tag{22}$$

where $c > 0$ defines the size of the tube.

Any control input should satisfy the following two robust HOCBF constraints in order to make the system state stay within the tube:

$$\begin{aligned} L_f^m b_1(\mathbf{x}) + L_g L_f^{m-1} b_1(\mathbf{x})\mathbf{u} + O(b_1(\mathbf{x})) \\ + \alpha_m(\psi_{1,m-1}(\mathbf{x})) \geq 0, \\ L_f^m b_2(\mathbf{x}) + L_g L_f^{m-1} b_2(\mathbf{x})\mathbf{u} + O(b_2(\mathbf{x})) \\ + \alpha_m(\psi_{2,m-1}(\mathbf{x})) \geq 0, \end{aligned} \tag{23}$$

where $\psi_{l,m-1}, l \in \{1,2\}$ are defined as in (11) for $b_1(\mathbf{x})$ and $b_2(\mathbf{x})$, respectively.

Finally, at each time step, we take the solution from the MPC (15), and combine MPC and CBF/HOCBF using the following optimization:

$$\min_{\mathbf{u}} ||\mathbf{u} - \mathbf{u}_R||^2, \quad \text{s.t., (23)} \tag{24}$$

where $\mathbf{u}_R$ is the reference control computed by the MPC (15). Thus, the CBF/HOCBF calculates a new control input $\mathbf{u}$, which is used to actuate the system. The above optimization is solved by discretizing the time [18], and only consider $\mathbf{u}$ as the decision variable at each time step while making the state as a constant within each time interval. Note that these constraints are linear in control since the state value is fixed at the beginning of the interval, therefore, each optimization problem is a quadratic program (QP) as the cost is quadratic. The optimal control obtained by solving each QP is applied at the current time step and held constant for the sampling interval. The state is updated using dynamics (10), and the procedure is repeated.

IV. Experiments and Results

In this section, we extensively conduct simulations and experiments using the surface vessel illustrated in Figure 1 to validate the tracking capabilities of the designed MPC-CBF control strategy.

We conduct a systematic comparison between the performance of the proposed MPC-CBF controller and our prior MPC controller [13] described by equations (15)-(19), with a focus on tracking error and control effort. We carry out identical simulation and physical experimental runs for both the MPC-CBF and benchmark MPC approaches. Also, it's worth noting that our trajectory tracking, as depicted in (14), is full-state tracking involving both pose and velocity tracking. However, due to space limit, this paper primarily focuses on the analysis of position tracking error. For position tracking error, we consider the Mean Absolute Error (MAE), defined as follows: $e_{\text{MAE}} = (\sum_{k=1}^{N} |\mathrm{e}_k|)/N$, where N is the total number of samples, and $\mathrm{e}_k = \left((x_k^{\mathrm{e}})^2 + (y_k^{\mathrm{e}})^2\right)^{\frac{1}{2}}$ represents the position error of the k-th sample. Regarding control effort evaluation, we use the Euclidean norm $||F_{\text{CE}}|| = \left(\sum_{k=1}^{N} (F_k^{\text{CE}})^2\right)^{\frac{1}{2}}$, where $F_k^{\text{CE}} = |f_{1,k}| + |f_{2,k}| + |f_{3,k}| + |f_{4,k}|$ denotes the total absolute force applied at each sample k.

To identify the unknown hydrodynamic parameters in the dynamic model, we employ a nonlinear least squares method based on the Trust Zone Reflection Algorithm [13]. For our vessel, the identified parameters are as follows: $m_{11} = 12$ kg, $m_{22} = 24$ kg, $m_{33} = 1.5$ kg m^2, $d_{11} = 6$ kg s^{-1}, $d_{22} = 8$ kg s^{-1}, and $d_{33} = 1.35$ kg m^2 s^{-1}. The simulations are conducted in Matlab 2022b, utilizing an Intel i9 CPU with 64GB RAM. Field tests on the surface vessel are carried out using its onboard Intel® NUC. The sine curve serves as the consistent reference trajectory for both simulations and experiments, while maintaining a constant forward speed of 0.2 m/s. Moreover, for both simulation and experimental setups with the surface vessel, a data sampling rate of 10 Hz is employed.

A. Simulations

In numerical simulations, we introduce model-based environmental disturbances to assess the MPC-CBF robustness. These disturbances are represented as $\boldsymbol{\tau}_{\text{env}} = \boldsymbol{\tau}_{\text{waves}} + \boldsymbol{\tau}_{\text{wind}} + (\mathbf{C}(\mathbf{v}_c) + \mathbf{D}(\mathbf{v}_c))\mathbf{v}_c$. Note that the current-induced forces involve current velocity $\mathbf{v}_c$, and Coriolis and Drag matrices.$\boldsymbol{\tau}_{\text{env}}$ is described in the following models [8], [25]:

Waves: Wave phenomena is modeled by a combination of two elements: zero-mean oscillatory motion and wave drift [25]. Using an approximation of the Pierson-Moskowitz spectrum, state-space models can be written in the shape of:

$$\dot{\mathbf{x}}_F = \begin{bmatrix} \dot{x}_{F1} \\ \dot{x}_{F2} \end{bmatrix} = \begin{bmatrix} 0 & 1 \\ -\omega_e^2 & -2\lambda_w\omega_e \end{bmatrix} \begin{bmatrix} x_{F1} \\ x_{F2} \end{bmatrix} + \begin{bmatrix} 0 \\ K_w \end{bmatrix} \omega_{F1} \tag{25}$$

$$F_{\text{wave}} = \begin{bmatrix} 0 & 1 \end{bmatrix} \begin{bmatrix} x_{F1} \\ x_{F2} \end{bmatrix} + d_F \tag{26}$$

$$\dot{\mathbf{x}}_N = \begin{bmatrix} \dot{x}_{N1} \\ \dot{x}_{N2} \end{bmatrix} = \begin{bmatrix} 0 & 1 \\ -\omega_e^2 & -2\lambda_w \omega_e \end{bmatrix} \begin{bmatrix} x_{N1} \\ x_{N2} \end{bmatrix} + \begin{bmatrix} 0 \\ K_w \end{bmatrix} \omega_{N1} \tag{27}$$

$$N_{\text{wave}} = \begin{bmatrix} 0 & 1 \end{bmatrix} \begin{bmatrix} x_{N1} \\ x_{N2} \end{bmatrix} + d_N \tag{28}$$

where F_{wave} is the wave force, N_{wave} is the wave moment, and $\dot{d}_F = \omega_{F2}, \dot{d}_N = \omega_{N2}$. There are random elements to generate the wave shape, in the form of Gaussian white noise signals $\omega_{F1}, \omega_{F2}, \omega_{N1}, \omega_{N2}$. See [8], [25] for a detailed description of the wave state-space representation. Then, the wave force and wave moment are introduced into the disturbance vector by computing:

$$\boldsymbol{\tau}_{\text{wave}} = \begin{bmatrix} X_{\text{wave}} \\ Y_{\text{wave}} \\ N_{\text{wave}} \end{bmatrix} = \begin{bmatrix} F_{\text{wave}} \cos(\beta_{\text{wave}} - \psi) \\ F_{\text{wave}} \sin(\beta_{\text{wave}} - \psi) \\ N_{\text{wave}} \end{bmatrix} \tag{29}$$

Wind: The wind speed and angle of attack (V_w, γ_{rw}, respectively) induce forces on moments on ASVs, depending on the aerodynamic characteristics of the system. The wind disturbance vector is given by:

$$\boldsymbol{\tau}_{\text{wind}} = \begin{bmatrix} X_{\text{wind}} \\ Y_{\text{wind}} \\ N_{\text{wind}} \end{bmatrix} = \frac{1}{2} \rho_a V_{rw}^2 \begin{bmatrix} C_X(\gamma_{rw}) A_{FW} \\ C_Y(\gamma_{rw}) A_{LW} \\ C_N(\gamma_{rw}) A_{LW} L_{OA} \end{bmatrix} \tag{30}$$

with the relative wind speed $V_{rw} = \sqrt{u_{rw}^2 + v_{rw}^2}$, considering the wind velocity vector $[u_{rw}, v_{rw}]^T = [V_w \cos(\beta_{\text{wind}} - \psi), V_w \sin(\beta_{\text{wind}} - \psi)]^T$, the wind durection β_{wind}, and the wind relative angle of attack $\gamma_{rw} = -\text{atan2}(v_{rw}, u_{rw})$. For more information on the aerodynamic coefficient compuation, go to [8], [25].

Currents: Commonly, currents are modeled with a Gauss-Markov proccess, under the assumption of irrotational currents [25], described by:

$$\dot{V}_c + \mu_c V_c = \omega_c \tag{31}$$

where V_c is the water current speed at direction β_c, ω_c is a Gaussian white noise process, and $\mu_c > 0$ is a parameter to change the current shape. Finally, the current velocity vector is written as $\mathbf{v}_c = [V_c \cos(\beta_c - \psi), V_c \sin(\beta_c - \psi), 0]^T$.

We present two studies to demonstrate the enhanced robustness achieved through the MPC-CBF strategy we propose. In the first study, we examine wave forces reaching approximately 1 N, a wind speed of 2.05 m/s, and currents extending to 0.2 m/s. The resulting disturbance is depicted in Figure 2 and is shown in the body frame throughout the trajectory. Figure 3 provides a comparison of the trajectory tracking performance in the presence of the environmental disturbances shown in Figure 2. It is clear that MPC-CBF outperforms MPC in terms of tracking error. To be specific, in this particular run with the disturbances, the tracking error of MPC-CBF is 0.20 m, whereas for MPC, it is 0.27 m, resulting in a 25.9% reduction in tracking error. Furthermore, Figure 4 illustrates a comparison of the corresponding control forces. The control effort for MPC is 48.81 N, whereas for

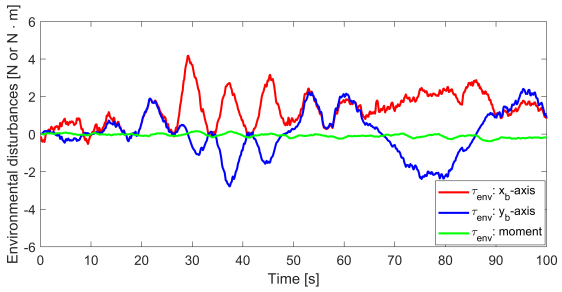

Fig. 2. Model-based disturbances from currents, waves, and winds, applied in the simulation.

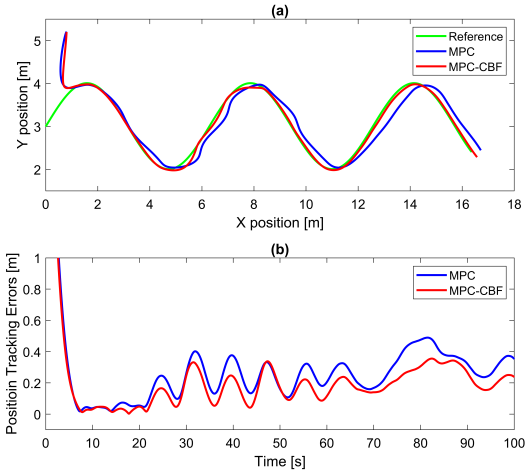

Fig. 3. Tracking performance comparison between MPC and MPC-CBF. (a) Position tracking; (b) Position tracking errors.

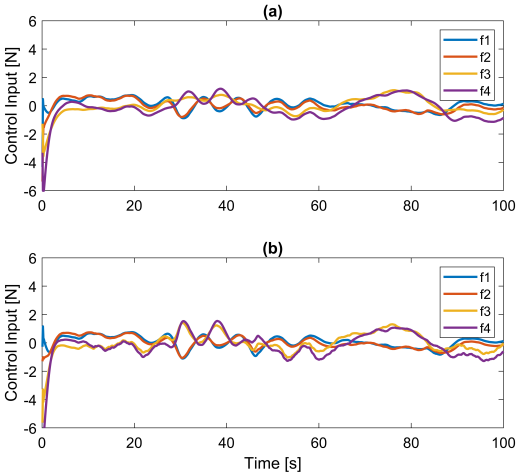

Fig. 4. Controls comparison between MPC and MPC-CBF. (a) MPC; (b) MPC-CBF.

MPC-CBF, it is slightly higher at 54.41 N. This represents a modest increase of 11.48% compared to MPC, which can be attributed to the improved robust performance achieved by MPC-CBF.

A second study was conducted to further distinguish the performance of MPC-CBF from that of MPC. In this study, a non-dimensional scale factor was introduced to scale the environmental disturbance $\boldsymbol{\tau}_{\text{env}}$. The disturbance signal

was built using waves-wind-currents model-based equations, and the scale factor was applied to modify the maginitude of the disturbance signal. 50 simulation runs were carried out, gradually increasing the scale factor from 0.7 to 2.5, significantly amplifying the disturbance. Figure 5 presents the tracking error and control effort for each scale factor. As environmental disturbances increase in magnitude, it

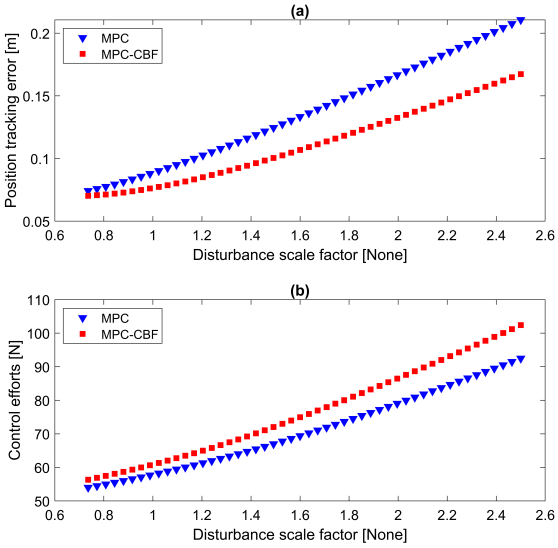

Fig. 5. Tracking error and control effort with increasing environmental disturbances in the simulation. (a) Tracking error, and (b) control effort.

becomes evident that both MPC and MPC-CBF experience an escalation in tracking errors. However, it's noteworthy that MPC-CBF consistently exhibits smaller tracking errors, accompanied by only a slight increase in control effort, and its capacity to enhance tracking becomes more pronounced as environmental disturbances grow in strength.

B. Experimental Results

We implemented the MPC-CBF control strategy on our surface vessel to follow reference trajectories within the Charles River in Boston, Massachusetts, USA. Both the MPC-CBF and MPC controllers were executed locally on the vessel's onboard computer, each with an approximate execution time of 1 ms. Furthermore, the vessel utilizes real-time SLAM (Simultaneous Localization and Mapping) [26], [27], making use of its onboard 3D LiDAR and IMU for estimating pose ($\boldsymbol{\eta}$) and velocity ($\mathbf{v}$).

Three experimental runs were conducted in the Charles River, employing both MPC-CBF and MPC controllers under varying environmental disturbance conditions. Figure 6 illustrates the comparative tracking performance between MPC-CBF and MPC. The performance comparison clearly demonstrates that MPC-CBF exhibits robustness improvements over MPC, particularly noticeable during the curves around $x = 8$ m and $x = 14$ m. To be specific, the average position error in the experiments for MPC-CBF is 0.14 m, while for MPC, it is 0.23 m, resulting in a reduction of 40.26%. Figure 7 presents the control effort for different runs after the time $t = 15$ s when all runs have reached

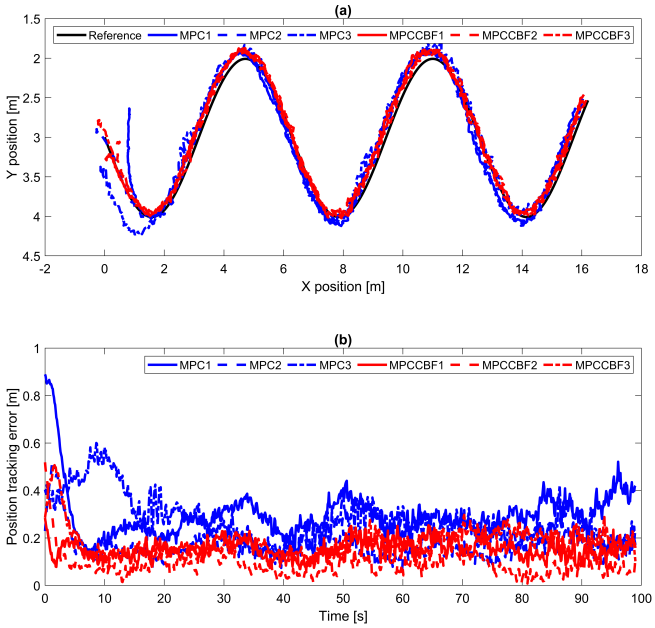

Fig. 6. Tracking performance comparison between MPC and MPC-CBF in Charles River. (a) Position tracking; (b) Position tracking errors.

a steady-state. The control effort for MPC is measured at

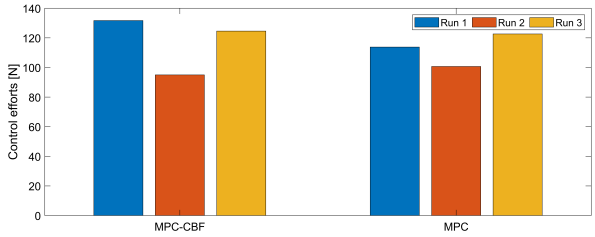

Fig. 7. Control efforts of MPC and MPC-CBF in the experiments.

112.38 N, while for MPC-CBF, it is 117.11 N. Consequently, the disparity between these control efforts is negligible. These experiments provide additional confirmation that in the presence of environmental disturbances, the proposed MPC-CBF approach exhibits greater robustness compared to MPC.

V. Conclusion and Future Work

In this paper, we introduce a control strategy that combines Model Predictive Control (MPC) with Control Barrier Functions (CBFs) to enhance trajectory tracking robustness in water environments subject to significant external disturbances. Our MPC-CBF strategy is validated through extensive testing, including simulations and real-world scenarios with natural water disturbances. Despite a minor increase in control effort, our approach demonstrates superior resilience in mitigating disturbances. Our future work involves extending this framework to account for factors such as model uncertainty and measurement noise. Furthermore, we plan to synergize our approach with perception-based techniques, addressing the intricacies of safe obstacle avoidance and thereby enhancing the applicability of our methodology in navigating unstructured water environments.

REFERENCES

[1] Y. Qiao, J. Yin, W. Wang, F. Duarte, J. Yang, and C. Ratti, "Survey of deep learning for autonomous surface vehicles in marine environments," *IEEE Transactions on Intelligent Transportation Systems*, vol. 24, no. 4, pp. 3678–3701, 2023.

[2] Z. Liu, Y. Zhang, X. Yu, and C. Yuan, "Unmanned surface vehicles: An overview of developments and challenges," *Annual Reviews in Control*, vol. 41, pp. 71–93, 2016.

[3] R. R. Murphy, E. Steimle, C. Griffin, C. Cullins, M. Hall, and K. Pratt, "Cooperative use of unmanned sea surface and micro aerial vehicles at hurricane wilma," *Journal of Field Robotics*, vol. 25, no. 3, pp. 164–180, 2008.

[4] M. Lindemuth, R. Murphy, E. Steimle, W. Armitage, K. Dreger, T. Elliot, M. Hall, D. Kalyadin, J. Kramer, M. Palankar, K. Pratt, and C. Griffin, "Sea robot-assisted inspection," *IEEE Robotics Automation Magazine*, vol. 18, no. 2, pp. 96–107, 2011.

[5] X. Bai, B. Li, X. Xu, and Y. Xiao, "A review of current research and advances in unmanned surface vehicles," *Journal of Marine Science and Application*, vol. 21, no. 2, pp. 47–58, 2022.

[6] W. Wang, D. Fernández-Gutiérrez, R. Doornbusch, J. Jordan, T. Shan, P. Leoni, N. Hagemann, J. K. Schiphorst, F. Duarte, C. Ratti, and D. Rus, "Roboat III: An autonomous surface vessel for urban transportation," *Journal of Field Robotics*, vol. 40, no. 8, pp. 1996–2009, 2023. [Online]. Available: https://onlinelibrary.wiley.com/doi/abs/10.1002/rob.22237

[7] W. Wang, X. Cao, A. Gonzalez-Garcia, L. Yin, N. Hagemann, Y. Qiao, C. Ratti, and D. Rus, "Deep reinforcement learning based tracking control of an autonomous surface vessel in natural waters," in *2023 IEEE International Conference on Robotics and Automation (ICRA)*, 2023, pp. 3109–3115.

[8] A. Gonzalez-Garcia and H. Castañeda, "Adaptive integral terminal super-twisting with finite-time convergence for an unmanned surface vehicle under disturbances," *International Journal of Robust and Nonlinear Control*, vol. 32, no. 18, pp. 10 271–10 291, 2022.

[9] S. Souissi and M. Boukattaya, "Time-varying nonsingular terminal sliding mode control of autonomous surface vehicle with predefined convergence time," *Ocean Engineering*, vol. 263, p. 112264, 2022.

[10] C. Zhang and S. Yu, "Disturbance observer-based prescribed performance super-twisting sliding mode control for autonomous surface vessels," *ISA Transactions*, 2022.

[11] Y. Weng and N. Wang, "Data-driven robust backstepping control of unmanned surface vehicles," *International Journal of Robust and Nonlinear Control*, vol. 30, no. 9, pp. 3624–3638, 2020.

[12] N. Wang, Y. Gao, and X. Zhang, "Data-driven performance-prescribed reinforcement learning control of an unmanned surface vehicle," *IEEE Transactions on Neural Networks and Learning Systems*, vol. 32, no. 12, pp. 5456–5467, 2021.

[13] W. Wang, L. Mateos, S. Park, P. Leoni, B. Gheneti, F. Duarte, C. Ratti, and D. Rus, "Design, modeling, and nonlinear model predictive tracking control of a novel autonomous surface vehicle," in *Proc. 2018 IEEE Int. Conf. Robot. Autom*, 2018, pp. 6189–6196.

[14] W. Wang, N. Hagemann, C. Ratti, and D. Rus, "Adaptive nonlinear model predictive control for autonomous surface vessels with largely varying payload," in *2021 IEEE International Conference on Robotics and Automation (ICRA)*, 2021, pp. 7337–7343.

[15] K. P. Tee, S. S. Ge, and E. H. Tay, "Barrier lyapunov functions for the control of output-constrained nonlinear systems," *Automatica*, vol. 45, no. 4, pp. 918–927, 2009.

[16] P. Wieland and F. Allgower, "Constructive safety using control barrier functions," in *Proc. of 7th IFAC Symposium on Nonlinear Control System*, 2007.

[17] S. P. Boyd and L. Vandenberghe, *Convex optimization*. New York: Cambridge university press, 2004.

[18] A. D. Ames, J. W. Grizzle, and P. Tabuada, "Control barrier function based quadratic programs with application to adaptive cruise control," in *Proc. of 53rd IEEE Conference on Decision and Control*, 2014, pp. 6271–6278.

[19] P. Glotfelter, J. Cortes, and M. Egerstedt, "Nonsmooth barrier functions with applications to multi-robot systems," *IEEE control systems letters*, vol. 1, no. 2, pp. 310–315, 2017.

[20] W. Xiao and C. Belta, "Control barrier functions for systems with high relative degree," in *Proc. of 58th IEEE Conference on Decision and Control*, Nice, France, 2019, pp. 474–479.

[21] W. Xiao and C. Belta, "High-order control barrier functions," *IEEE Transactions on Automatic Control*, vol. 67, no. 7, pp. 3655–3662, 2021.

[22] L. Lindemann and D. V. Dimarogonas, "Control barrier functions for multi-agent systems under conflicting local signal temporal logic tasks," *IEEE Control Systems Letters*, vol. 3, no. 3, pp. 757–762, 2019.

[23] H. K. Khalil, *Nonlinear Systems*. Prentice Hall, third edition, 2002.

[24] B. Houska, H. Ferreau, and M. Diehl, "ACADO Toolkit – An Open Source Framework for Automatic Control and Dynamic Optimization," *Optimal Control Applications and Methods*, vol. 32, no. 3, pp. 298–312, 2011.

[25] T. I. Fossen, *Handbook of Marine Craft Hydrodynamics and Motion Control*. John Wiley & Sons, 2011.

[26] T. Shan, B. Englot, D. Meyers, W. Wang, C. Ratti, and D. Rus, "LIO-SAM: Tightly-coupled lidar inertial odometry via smoothing and mapping," in *2020 IEEE/RSJ International Conference on Intelligent Robots and Systems (IROS)*, 2020, pp. 5135–5142.

[27] W. Wang, T. Shan, P. Leoni, D. Fernández-Gutiérrez, D. Meyers, C. Ratti, and D. Rus, "Roboat II: A novel autonomous surface vessel for urban environments," in *2020 IEEE/RSJ International Conference on Intelligent Robots and Systems (IROS)*, 2020, pp. 1740–1747.